

Article

Preparation of Glass-Ceramics in the R_2O - Bi_2O_3 - B_2O_3 - SiO_2 System Applied in Automobile Glass Enamel

Tianguai Zhao ^{1,2}, Wei Wang ¹, Kun Liu ¹, Li Liu ², Weixia Dong ¹, Qifu Bao ^{1,*}, Heliang Xu ² and Jianer Zhou ^{1,*}¹ School of Materials Science and Engineering, Jingdezhen Ceramic University, Jingdezhen 333403, China; tgzhao524@163.com (T.Z.)² Jiangsu Baifu Technology Co., Ltd., Yixing 214200, China

* Correspondence: dwxbqf0727@163.com (Q.B.); lp0518@126.com (J.Z.)

Abstract: Environmental deterioration has put higher requirements on the acid resistance of automotive glass enamel. The present paper aims to prepare acid-resistant glass-ceramics used in automobile glass enamel. Base glasses with the compositions $15R_2O$ - xBi_2O_3 - $10B_2O_3$ - $(75-x)SiO_2$ (R_2O is a mixture of Li_2O , Na_2O , and K_2O (1:1:1, molar ratio), where $x = 10, 15, 20, 25$, and 30 , respectively) was prepared by the melt-quenching method, and glass-ceramics were prepared by their controlling crystallization heat treatment. Crystallization behavior and crystallization ability of base glasses were investigated using the thermal stability parameter (S), the crystallization kinetics calculation results of base glasses, as well as the phase identification results of the heat-treated samples. The effects of the heat treatment temperature on the micromorphology and acid resistance of the heat-treated glasses were also investigated. Then, the optimized glass ceramic was used to prepare automotive glass enamel. The results indicate that: (I) with the increase of Bi_2O_3/SiO_2 ratio, the characteristic temperature of the base glass decreases, the coefficient of thermal expansion (CTE) and crystallization ability increases significantly, the crystallization temperature range becomes wider; (II) the crystallization activation energy of base glasses are in the range of 169~264 kJ/mol; (III) Bi_2SiO_5 and $Bi_2O_2SiO_3$ metastable phases are mainly precipitated when the crystallization temperature is between 530 °C and 650 °C, while only $Bi_4Si_3O_{12}$ phase is precipitated when the crystallization temperature is above 650 °C; (IV) crystallinity of base glass increases significantly with increasing heat treatment temperature, which is beneficial to improve the acid resistance of heat treated products; (V) automotive glass enamel was prepared by mixing $15R_2O$ - $25Bi_2O_3$ - $10B_2O_3$ - $50SiO_2$ glass-ceramic powder with copper-chrome black and varnish, and then printed on the automobile glass substrate. All the properties of the sintered enamel can meet the market requirements, and the acid resistance of our product is better than that of market products.

Keywords: R_2O - Bi_2O_3 - B_2O_3 - SiO_2 glass; heat treatment; glass-ceramics; automotive glass enamel

Citation: Zhao, T.; Wang, W.; Liu, K.; Liu, L.; Dong, W.; Bao, Q.; Xu, H.; Zhou, J. Preparation of Glass-Ceramics in the R_2O - Bi_2O_3 - B_2O_3 - SiO_2 System Applied in Automobile Glass Enamel. *Inorganics* **2023**, *11*, 166. <https://doi.org/10.3390/inorganics11040166>

Academic Editor: Kenneth J.D. MacKenzie

Received: 8 March 2023

Revised: 11 April 2023

Accepted: 13 April 2023

Published: 14 April 2023



Copyright: © 2023 by the authors. Licensee MDPI, Basel, Switzerland. This article is an open access article distributed under the terms and conditions of the Creative Commons Attribution (CC BY) license (<https://creativecommons.org/licenses/by/4.0/>).

1. Introduction

Since 2009, China has become the world's largest producer and seller of automobiles, and the number of automobiles in China will reach 260 million by 2022 [1–4]. The huge automotive market has driven the demand for glass enamel, a supporting product for automobiles [5]. Enamel paste consists of low melting point glass powder, inorganic black pigment, and varnish, usually printed around the glass of the car, commonly known as the “black frame” [6,7]. Automotive glass enamel not only has a decorative function but can also enhance the bonding between the glass and car body and reduce ultraviolet transmittance [7,8]. Glass enamel contains 55–70 wt.% low melting point glass powder, whose properties determine the sintering temperature, color, and chemical stability of the glass enamel [9,10]. Currently, most glass enamels used in the market are prepared from lead-based glass powder [11,12]. Lead-based glass has the advantages of a low glass transition temperature (T_g), a wide range of adjustable coefficient of thermal expansion

(CTE), and a high refractive index [13,14]. However, the volatilization of PbO in the process of lead-based glass production and the leaching of Pb²⁺ ions after the disposal of lead-containing products will cause serious harm to human health and the environment [15–18]. With the gradual deterioration of the atmospheric environment, the acid rain phenomenon appears in different degrees all over the world, which puts forward higher requirements for the chemical stability of automotive glass enamel, especially acid resistance [19,20]. Nevertheless, the acid resistance of the existing automobile glass enamel on the market is generally not high, and problems such as fading or shedding often occur during service [5,7]. In order to solve the above problems, it is urgent to develop a new type of lead-free enamel with excellent acid resistance and CTE similar to that of automobile glass substrate. Bismuth and lead have very similar properties because they are adjacent, have a similar molecular weight, and have a similar electronic structure [21–23]. The structure and properties of bismuth glass have been studied in depth in order to investigate the possibility of bismuth glass replacing lead-based glass. Studies have shown that bismuth glass with low T_g is usually not chemically stable, which makes it difficult to meet the requirements of automotive glass enamel [24,25]. Thus far, there are two main methods to improve the chemical stability of bismuthate glasses. One method is to strengthen the glass network by doping with oxide, especially rare metal doping, and to hinder the migration of metal ions with lower valence. For example, by adding 1~10% Ta₂O₅ or 2~6% Y₂O₃ to Na₂O-ZnO-Bi₂O₃-B₂O₃-Al₂O₃-SiO₂ glass, the resistance of the glass to 10% citric acid corrosion can be sharply improved from grade 4~5 to grade 1 (the highest grade) [26,27]. Adding 2% WO₃ to 20Li₂O-20Bi₂O₃-60B₂O₃ glass can reduce its dissolution rate (DR_{Water}) in water at 90 °C by two orders of magnitude (from 10⁻⁴ g·cm⁻²·min⁻¹ to 10⁻⁶ g·cm⁻²·min⁻¹) [20]. Although the chemical stability of bismuthate glass can be obviously improved by doping rare metal oxides, the cost of enamel production is increased due to the limited source of rare metal oxides. Another method to improve the chemical stability of bismuth-based low-melting-point glasses is to prepare their corresponding glass-ceramics. As we all know, compared with the corresponding base glass, the mechanical properties, thermal stability, and chemical stability of glass ceramic will usually be improved to a certain degree, and the degree of improvement depends on the type of precipitated phase, the crystallinity, and the microscopic morphology of the crystalline phase [28–31]. The dissolution rates (DR_{Acid}) of (65-x)Bi₂O₃-xZnO-30B₂O₃-5BaO (x = 40~60 mol%) glass-ceramics, with a large number of needle-like Bi₂ZnB₂O₇ crystals, in a 6 wt.% nitric acid solution at 90 °C are near 10⁻³ g·cm⁻²·min⁻¹ [32]. However, the DR_{Acid} of 40Bi₂O₃-30B₂O₃-(30-x)ZnO-xSrO (x = 0~15 mol%) glass-ceramics in sulfuric acid (6 wt.%) at 90 °C is as low as 10⁻⁵ g·cm⁻²·min⁻¹ [33]. Although these Bi₂O₃-B₂O₃-ZnO-SrO glass-ceramics have excellent acid resistance, they are not suitable for preparing glass enamel because their $\alpha_{30\sim300\text{ }^\circ\text{C}}$ values are near $11.15 \times 10^{-6}/^\circ\text{C}$, which is much higher than that of automobile glass ($\alpha_{30\sim300\text{ }^\circ\text{C}} = (8\sim10) \times 10^{-6}/^\circ\text{C}$).

In fact, low melting point glass for glass enamel does not need to have a very low softening temperature because the plate glass used to print enamel needs to undergo a tempering process in order to improve strength before being used as window glass. The tempering process needs to be held at 720 °C for 210~300 s [34]. Glass with a drastically low softening temperature will be over-sintered at 720 °C, leading to the formation of air bubbles that reduce the adhesion of the enamel layer. Generally, bismuth silicate glass is more suitable for preparing glass enamel than bismuth borate glass since it has much higher chemical stability and softening temperature [23,35]. The structure and properties of bismuth-silicate glasses, mainly the Bi₂O₃-B₂O₃-SiO₂-R_xO_y (R = Na, K, Zn, and Ca) systems, have been reported [36–38]. According to our knowledge, bismuth-silicate glasses and glass-ceramics are mainly used as sealing materials, and their application in glass enamel is rare. Defects can affect the number of carriers in glass, thereby affecting its electrical and optical properties [39–41], but this aspect of performance does not need to be considered when applied to enamels. In the present paper, glasses in the R₂O-Bi₂O₃-B₂O₃-SiO₂ system are proposed as the base glasses to prepare the corresponding

glass-ceramics. R_2O - Bi_2O_3 - B_2O_3 - SiO_2 glass-ceramic powder is homogeneously mixed with inorganic pigment and varnish, and the mixture is screen printed on the flat glass. The flat glass is then tempered. The possibility of practical application of the enamel in automotive windows will be evaluated by studying the various properties of the enamel products.

2. Experimental Procedure

2.1. Preparation of Automotive Glass Enamel

$15R_2O$ - xBi_2O_3 - $10B_2O_3$ - $(75-x)SiO_2$ ($x = 10, 15, 20, 25,$ and 30) glasses were prepared by the melt-cooling method; their detailed compositions are listed in Table 1. R_2O is a mixture of Li_2O , Na_2O , and K_2O (1:1:1, molar ratio). All raw materials are analytically pure; alkali oxides (R_2O) were introduced with the corresponding carbonate; B_2O_3 was introduced with boric acid; and Bi_2O_3 and SiO_2 were introduced in the form of oxides. According to the stoichiometric ratio of each sample in Table 1, a 200 g batch was prepared and melted in a corundum crucible. The batch was melted at $1250\text{ }^\circ\text{C}$ for 1 h. Homogeneous melt was cast into a preheated stainless-steel mold, annealed at T_g for 1 h to release the residual stress, and then bulk glass was prepared after cooling. The bulk glass was crushed through a 200-mesh sieve to obtain glass powder for phase identification and differential thermal analysis. The corresponding glass-ceramics were prepared by controlled heat treatment on bulk glasses. The heat treatment schedule of each sample was determined according to its differential thermal analysis (DTA) curve.

Table 1. Compositions of base glasses.

Sample Codes	R_2O (mol%)	Bi_2O_3 (mol%)	B_2O_3 (mol%)	SiO_2 (mol%)
A1	15	10	10	65
A2	15	15	10	60
A3	15	20	10	55
A4	15	25	10	50
A5	15	30	10	45

The enamel paste was obtained by mixing glass-ceramic fine powder ($D_{90} = 7\text{--}8\text{ }\mu\text{m}$), inorganic black pigment ($CuCr_2O_4$, $D_{90} = 1.5\text{--}2.0\text{ }\mu\text{m}$), and varnish (acrylic resin, glycerol, and diethylene glycol butyl ether mixed) at a mass ratio of 60:20:20. The enamel was printed on the automobile glass substrate through a 250-mesh screen, and the thickness of the enamel layer was controlled at $22\text{--}24\text{ }\mu\text{m}$. The glass substrate printed with enamel was tempered at $720\text{ }^\circ\text{C}$ for about 210 s to obtain the final product. The preparation process and application of automobile glass enamel are shown in Figure 1.

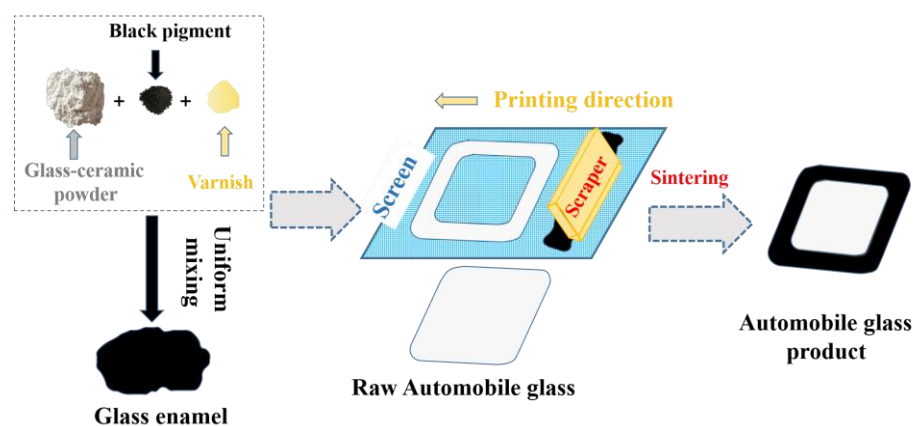


Figure 1. The preparation process and application of automobile glass enamel.

2.2. Performance Testing and Characterization of Materials

Phase identification of base glasses and heat-treated glasses was carried out by an X-ray diffractometer (Bruker D8 advance, Germany), and the scanning range of 2θ angle

was 10~80°. The CTE of bulk base glasses and some glass-ceramics was measured by a coefficient of thermal expansion instrument (DIL 402C, NETZSCH, Germany) with a heating rate of 5 °C/min. The average CTE values from 30 °C to 300 °C (α_{30-300} °C) of samples were used to investigate their dependence on the compositions. The glass transition temperature ($T_{g(Dil)}$) and softening temperature (T_f) of each base glass were derived from its CTE curve, and their methods of evaluation are indicated in the curve.

Differential thermal analysis (DTA) curves were recorded by an analyzer (ZCT-B, Beijing Jingyi Gaoke Instrument company) at a heating rate of 5 °C/min from 25 °C to 900 °C with Al₂O₃ as the reference material. Glass transition temperature ($T_{g(DTA)}$), onset crystallization temperature (T_x), and the crystallization peak temperature of base glass were determined according to the DTA curve, and their methods of evaluation are indicated in the curve. The thermal stability parameter (S) was used to judge the thermal stability of each base glass, and its calculation equation is shown in Equation (1) [42–44]. The larger the S value, the higher the thermal stability. It is generally considered that glass with $S \geq 100$ °C has relatively high thermal stability [45,46].

$$S = T_x - T_{g(DTA)} \quad (1)$$

In order to study the crystallization kinetics of A4 base glass, its DTA curves were measured at heating rates of 5 °C/min, 10 °C/min, 15 °C/min, and 20 °C/min, respectively. Kissinger's equation (Formula (2)) [47] was used to calculate its crystallization activation energy, and Formula (3) [47,48] was used to calculate its crystal growth index (n). In Equation (2), E_c is the crystallization activation energy, β is the heating rate, R is the gas constant, and T_p is the crystallization peak temperature. A straight line can be obtained by plotting $\ln\left(\frac{\beta}{T_p^2}\right)$ to $1/RT_p$, and the crystallization activation energy E_c can be obtained according to the slope of this line. In Equation (3), ΔT is the half-peak width of the crystallization exothermic peak, which can be obtained by Gaussian fitting.

$$\ln\left(\frac{\beta}{T_p^2}\right) = -\frac{E_c}{RT_p} + constant \quad (2)$$

$$n = \frac{2.5}{\Delta T} \cdot \frac{T_c^2}{(E_c/R)} \quad (3)$$

Glass-ceramics and the tempered automotive glass printed with enamel were immersed in a 6 wt.% HNO₃ solution at 90 °C for 48 h. The acid resistance is evaluated according to the leaching rate value (DR_{Acid}) of each sample in an acid solution. The smaller the DR_{Acid} value indicates the better the acid resistance of the sample, which is calculated by Equation (4) [32,33], where ΔW is the mass difference between the glass-ceramic before and after acid immersion (g), A is the surface area of the sample (cm²), and t is the immersion time (min). The microstructure of each heat-treated sample before and after corrosion in an acid solution was observed by a scanning electron microscope (JSM-6700F, Nippon Electronics).

$$DR_{Acid} = \frac{\Delta W}{A \times t} \quad (4)$$

The Cross-Cut Tester (5152, BYK, Germany) was used to test the adhesion of the sintered enamel. The smaller the ISO grade, the better the bonding between the enamel layer and the glass, and grade 0 was the optimal grade. The colorimeter (CM-26d, Konica Minolta, Japan) was used to test the chroma (L , a , and b) of the enamel after sintering through the glass surface. The smaller the L value, the darker the color. The optical density meter (PRO-361, Xianyang Prospect Instrument Company) was used to test the covering rate of the sintered enamel. A larger OD value means lower transmittance of the enamel layer and stronger shading ability. An intelligent gloss meter (KGZ-1C, Xiangtan Xiangyi Company) was used to test the gloss of sintered enamel. The roughness of the enamel

surface after sintering was tested by a roughness meter (SL-030B, Beijing Jitai Company). The surface tension of the sintered enamel was tested with a Dyne Pen (Aisa, USA).

3. Results and Discussion

3.1. Glass Forming Ability and Thermal Properties

The XRD patterns of the samples prepared by the melt-cooling method are shown in Figure 2. As shown in Figure 2, all samples are vitreous because a wide scattering peak in the range of $2\theta = 25\sim 35^\circ$ can be observed in each pattern, indicating that all samples were not crystallized during the preparation process [49]. It also reflects that each composition in Table 1 has strong glass-forming ability. Figure 3 shows the CTE curves for all glass samples, and the $\alpha_{30\sim 300\text{ }^\circ\text{C}}$, $T_{g(\text{Dil})}$, and T_f values are listed in Table 2. T_g reflects the tightness of the glass network structure [50], and the decrease in its value indicates that the integrity of the glass network structure becomes worse. The bond energy of Bi-O is lower than that of Si-O. As Bi_2O_3 gradually replaces SiO_2 , the content of the Bi-O bond and non-bridged oxygen bond in the glass gradually increases, leading to a decrease in the tightness of the glass network connection, thereby reducing the characteristic temperature of the glass and increasing the CTE.

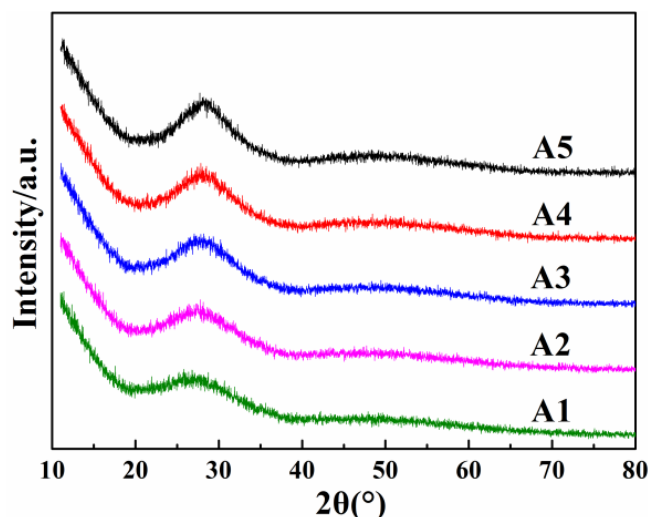


Figure 2. XRD patterns of A1–A5 samples.

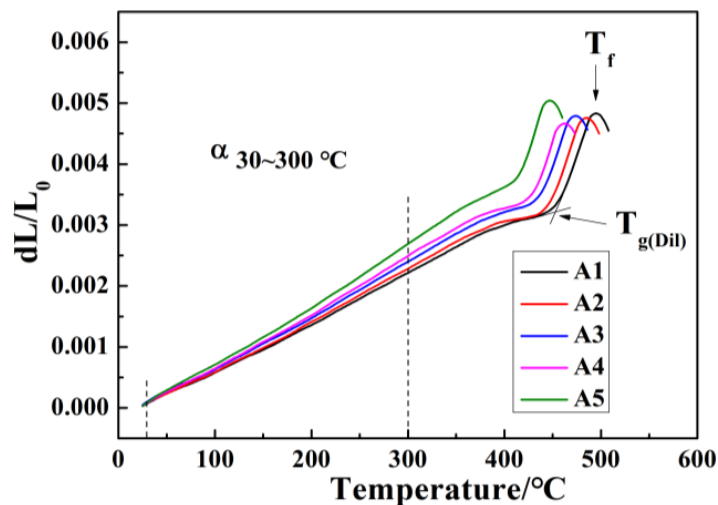
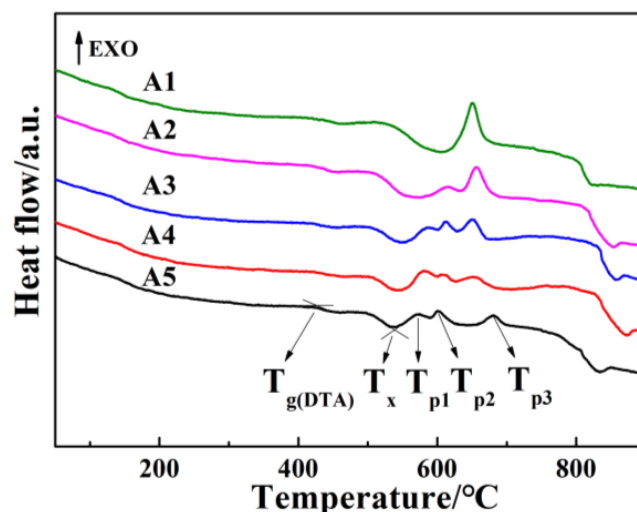


Figure 3. CTE curves of base glasses.

Table 2. $\alpha_{30\sim 300}$ °C, T_g (Dil), and T_f values of base glasses.

Sample Codes	$\alpha_{30\sim 300}$ °C ($\pm 0.2 \times 10^{-6}/^\circ\text{C}$)	$T_{g(Dil)}$ (± 5 °C)	T_f (± 5 °C)
A1	7.93	449	497
A2	8.32	441	484
A3	8.77	435	473
A4	9.05	430	462
A5	9.89	419	446

Figure 4 shows the DTA curves of all base glasses; their $T_{g(DTA)}$, T_x , T_p , and S values are listed in Table 3. As the $\text{Bi}_2\text{O}_3/\text{SiO}_2$ ratio increases from 1:6.5 in A1 to 1:1.5 in A5, the thermal properties of base glasses show a regular variation: $T_{g(DTA)}$ decreases from 442 °C to 421 °C, and the variation trends of $T_{g(DTA)}$ and $T_{g(Dil)}$ are quite similar; the T_x decreases significantly from 617 °C to 539 °C; the number of crystallization exothermic peaks varies from 1 in A1 to 2 in A2 to 3 in A3–A5, indicating that the range of crystallization temperatures of samples is obviously wider; and the value of S decreases from 175 °C to 118 °C, indicating that the thermal stability of the base glass decreases significantly and it becomes easy to crystallize. It is well known that Bi^{3+} has high polarizability, and glasses with high contents of Bi_2O_3 are easy to crystallize [51,52]. It is worth noting that the S values of A1–A5 base glasses are greater than 100 °C, which indicates they have relatively good thermal stability and strong glass-forming ability. This result is consistent with the XRD identification results of base glasses. The difference between $T_{g(DTA)}$ and $T_{g(Dil)}$ is mainly due to the fact that the DTA and CTE tests were carried out on bulk and powder glass samples, respectively.

**Figure 4.** DTA curves of A1–A5 base glasses.**Table 3.** Characteristic temperatures and thermal stability parameters of base glasses.

Sample Codes	$T_{g(DTA)}$ (± 5 °C)	T_x (± 5 °C)	T_{p1} (± 5 °C)	T_{p2} (± 5 °C)	T_{p3} (± 5 °C)	S (± 5 °C)
A1	442	617	653	/	/	175
A2	437	578	615	654	/	141
A3	427	554	585	611	651	127
A4	426	545	574	606	659	119
A5	421	539	573	602	681	118

It is well known that the CTE values of flat glasses fluctuate within a certain range with variations in their compositions. $\alpha_{30\sim 300}$ °C values of flat glass and tempered glass are usually in the range of $(8\sim 10) \times 10^{-6}/^\circ\text{C}$ [53]. The $\alpha_{30\sim 300}$ °C values of the glass samples prepared in the present paper basically fall in this range, indicating that the

CTE of $R_2O-Bi_2O_3-B_2O_3-SiO_2$ glass and flat glass are basically matched. If A1–A5 base glasses are used for automotive enamel, they need to be tempered at 720 °C, and their softening temperatures (450~500 °C range) are relatively low. Therefore, we considered preparing $R_2O-Bi_2O_3-B_2O_3-SiO_2$ glass-ceramics through controlled crystallization heat treatment of base glasses. In the $Bi_2O_3-SiO_2$ system, glass ceramic is more heat-resistant than its base glass, while its CTE value is usually lower than that of the corresponding base glass. The residual glassy phases that exist in glass-ceramic can play a role in firmly adhering black pigment to the automobile glass matrix. This is the main reason that we use $R_2O-Bi_2O_3-B_2O_3-SiO_2$ glass-ceramic powder to prepare enamel.

3.2. Crystallization Kinetics Analysis of Base Glass

With increasing Bi_2O_3/SiO_2 ratio, S value gradually decreases, indicating that the crystallization trend of the glass increases, which is unfavorable to the preparation of the glass but beneficial to the preparation of the glass-ceramics. Before the preparation of $R_2O-Bi_2O_3-B_2O_3-SiO_2$ glass-ceramics, we took an A4 sample as an example to investigate its crystallization kinetics. DTA tests were carried out on A4 glass powder at 5 °C/min, 10 °C/min, 15 °C/min, and 20 °C/min, respectively. DTA curves obtained at different heating rates are shown in Figure 5. The peak temperatures of each sample's crystallization exothermic peak originated from DTA curves in Figure 5 and are listed in Table 4. As shown in Figure 5 and Table 4, with the increase in heating rate from 5 °C/min to 20 °C/min: (I) the intensity of the crystallization exothermic peak is obviously enhanced; (II) the shape of each DTA curve is quite similar, and each curve has three exothermic peaks, and their relative strength varies little; (III) the peak temperature of each crystallization exothermic peak increases obviously, which is mainly due to the hysteresis effect of heat transfer [54]. The dependence of $\ln\left(\frac{\beta}{T_c^2}\right)$ on $1/RT_p$ is shown in Figure 6. The calculation result of crystallization activation energy corresponding to each crystallization exothermic peak of the A4 sample is $E_{c1} = 208.4$ kJ/mol, $E_{c2} = 169.4$ kJ/mol, and $E_{c3} = 263.4$ kJ/mol, respectively. The three Avrami indexes calculated are $n_1 = 2.06$, $n_2 = 2.58$, and $n_3 = 2.23$, respectively. Crystal growth index calculation results indicate that the crystals are volume nucleated, grow in two dimensions, and crystallize simultaneously on the surface and inside the glass [47,55].

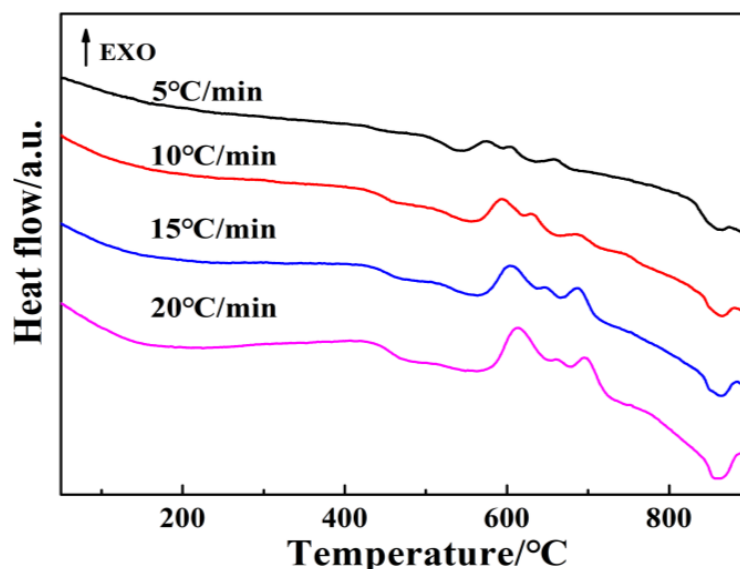
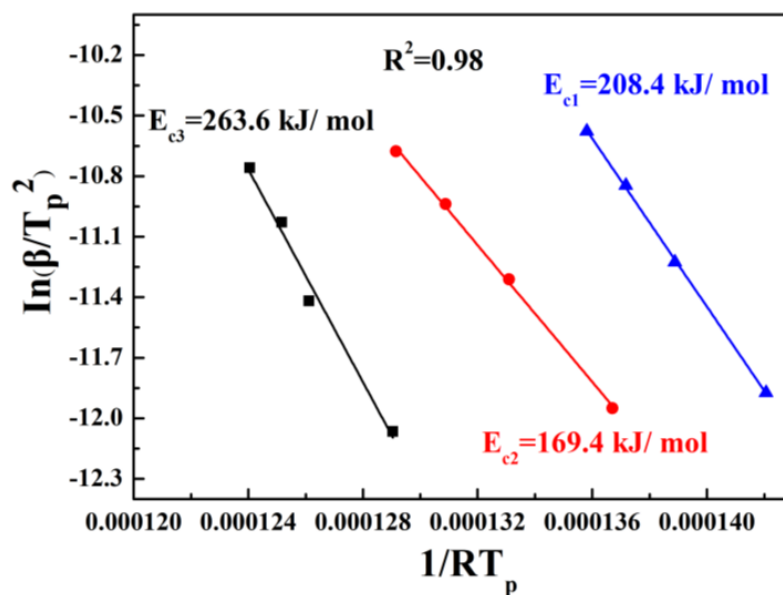


Figure 5. DTA curves of the A4 glass heated at different rates.

Table 4. T_p , E_c , and n values of A4 base glass heated at different rates.

Heating Rates (°C/min)	T_{p1} (± 5 °C)	T_{p2} (± 5 °C)	T_{p3} (± 5 °C)
5	574	606	659
10	593	630	681
15	604	646	688
20	613	658	696
E_c and n values			
E_c (kJ/mol)	$E_{c1} = 208.4$	$E_{c2} = 169.4$	$E_{c3} = 263.6$
n	2.06	2.58	2.23

**Figure 6.** Kissinger kinetic plots of A4 glass.

3.3. Preparation and Properties of Glass-Ceramics

3.3.1. Phase Identification of Heat-Treated Base Glasses

According to the DTA curves of base glasses in Figure 4, their crystallization heat treatment schedules were determined. For each base glass, it was heated at the onset crystallization temperature and the crystallization peak temperature, respectively. The XRD patterns of all heat-treated samples are shown in Figure 7. The detailed heat treatment schedules and crystalline phases precipitated in each base glass are listed in Table 5. The samples prepared by heating the base glass near the onset crystallization temperature for 2 h are amorphous, such as the A2-1, A3-1, A4-1, and A5-1 samples. A small amount of crystallization was detected in A1-1. For A2–A5 base glasses with multiple crystallization and exothermic peaks, the crystallinity of the samples obtained after heat treatment at T_{p1} for 2 h is significantly higher than that of the samples heated at T_x for the same time. However, the crystallinity was still very low, and the prepared samples were not strictly glass-ceramics, such as the A2-2, A3-2, A4-2, and A5-2 samples. If the crystallinity is to be improved, the heating time under T_{p1} should be extended. The main crystalline phase of these samples heated at T_{p1} is $\text{Bi}_2\text{O}_2\text{SiO}_3$, and a small amount of Bi_2SiO_5 crystals were detected in them except for A2-2. For A3–A5-based glass, when the heat treatment temperature is increased to T_{p2} , the crystallinity of each sample is significantly improved, and a new crystalline phase ($\text{Bi}_4\text{Si}_3\text{O}_{12}$) is precipitated. The crystallization degree of A3-3, A4-3, and A5-3 samples is relatively high, and they have three kinds of crystalline phases, including $\text{Bi}_2\text{O}_2\text{SiO}_3$, Bi_2SiO_5 , and $\text{Bi}_4\text{Si}_3\text{O}_{12}$. All samples obtained by heating base glasses at the peak temperature of the last crystallization exothermic peak for 2 h have high crystallinity, including A1-2, A2-3, A3-4, A4-4, and A5-4 samples. These samples are glass-ceramics, and only $\text{Bi}_4\text{Si}_3\text{O}_{12}$ crystals are detected.

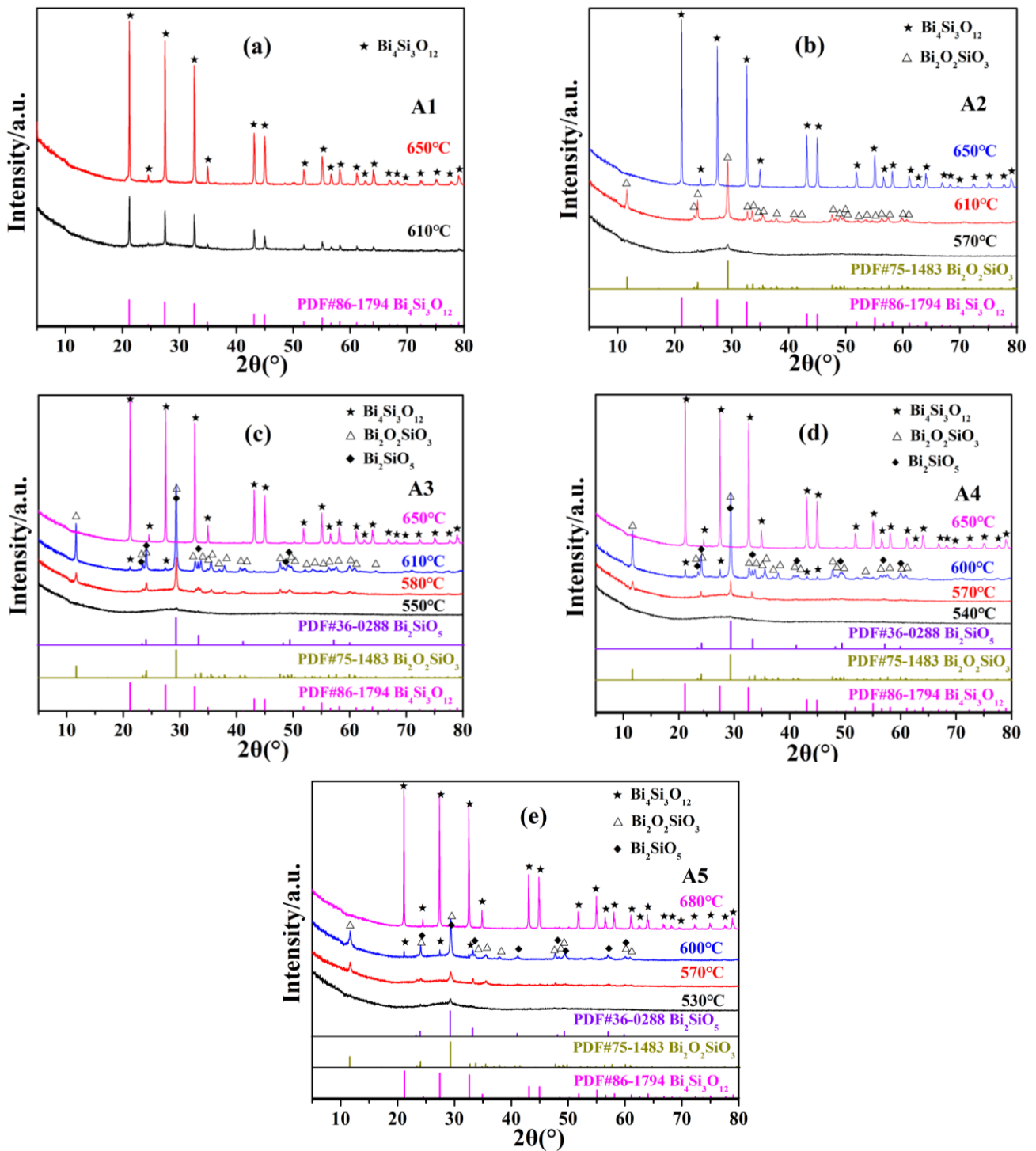


Figure 7. XRD patterns of all heat-treated base glasses. (a) A1, (b) A2, (c) A3, (d) A4, (e) A5.

In summary, the type of crystalline phase in heat-treated base glass depends on the number of crystallization exothermic peaks. According to the XRD results of heated samples, it is reasonably concluded that Bi_2SiO_5 and $\text{Bi}_2\text{O}_2\text{SiO}_3$ crystals are metastable transition phases [56,57], and all of them transform into stable $\text{Bi}_4\text{Si}_3\text{O}_{12}$ crystal phases with the increase of heat treatment temperature. Combined with XRD and crystallization kinetics analysis, we infer that the first crystallization exothermic peak (T_{p1}) in the DTA curve of the A4 sample is caused by the precipitation of Bi_2SiO_5 crystal phase; the second crystallization exothermic peak (T_{p2}) results from the precipitation of $\text{Bi}_2\text{O}_2\text{SiO}_3$ crystal

phase; and the third crystallization exothermic peak (T_{p3}) is due to the precipitation of $\text{Bi}_4\text{Si}_3\text{O}_{12}$ crystal phase. Bi_2SiO_5 and $\text{Bi}_2\text{O}_2\text{SiO}_3$ crystals have lower activation energies, and they are easy to precipitate. $\text{Bi}_4\text{Si}_3\text{O}_{12}$ crystals have a higher activation energy, and their precipitation from the base glass requires a much higher temperature.

Table 5. Heat treatment schedules of A1–A5 base glasses, DR_{Acid} values, and crystalline phases in heated base glass.

Base Glass Codes	Heat Treatment Schedules	Heated Base Glass Codes	Crystalline Phases	DR_{Acid} ($\times 10^{-5} \text{ g}\cdot\text{cm}^{-2}\cdot\text{min}^{-1}$)
A1	610 °C/2 h	A1-1	$\text{Bi}_4\text{Si}_3\text{O}_{12}$	2.01
	650 °C/2 h	A1-2	$\text{Bi}_4\text{Si}_3\text{O}_{12}$	0.38
A2	570 °C/2 h	A2-1	No crystals	3.32
	610 °C/2 h	A2-2	$\text{Bi}_2\text{O}_2\text{SiO}_3$	1.38
	650 °C/2 h	A2-3	$\text{Bi}_4\text{Si}_3\text{O}_{12}$	0.38
A3	550 °C/2 h	A3-1	No crystals	6.30
				2.66
				1.82
	580 °C/2 h	A3-2	$\text{Bi}_2\text{O}_2\text{SiO}_3$ (major phase); Bi_2SiO_5 (minor phase)	0.52
				2.66
				1.82
610 °C/2 h	A3-3	$\text{Bi}_2\text{O}_2\text{SiO}_3$ (major phase); Bi_2SiO_5 (secondary phase); $\text{Bi}_4\text{Si}_3\text{O}_{12}$ (minor phase)	0.52	
			0.52	
			0.52	
A4	540 °C/2 h	A4-1	No crystals	9.63
	570 °C/2 h	A4-2	$\text{Bi}_2\text{O}_2\text{SiO}_3$ (major phase); Bi_2SiO_5 (minor phase)	4.14
	600 °C/2 h	A4-3	$\text{Bi}_2\text{O}_2\text{SiO}_3$ (major phase); Bi_2SiO_5 (secondary phase); $\text{Bi}_4\text{Si}_3\text{O}_{12}$ (minor phase)	2.95
				0.83
	650 °C/2 h	A4-4	$\text{Bi}_4\text{Si}_3\text{O}_{12}$	0.83
A5	530 °C/2 h	A5-1	No crystals	12.24
	570 °C/2 h	A5-2	$\text{Bi}_2\text{O}_2\text{SiO}_3$ (major phase); Bi_2SiO_5 (minor phase)	8.14
	600 °C/2 h	A5-3	$\text{Bi}_2\text{O}_2\text{SiO}_3$ (major phase); Bi_2SiO_5 (secondary phase); $\text{Bi}_4\text{Si}_3\text{O}_{12}$ (minor phase)	5.61
2.45				
	680 °C/2 h	A5-4	$\text{Bi}_4\text{Si}_3\text{O}_{12}$	2.45

3.3.2. Microstructure and Properties of Heat-Treated Base Glasses

DR_{Acid} values of all heat-treated base glasses are shown in Table 5 and Figure 8. DR_{Acid} value decreases by an order of magnitude with increasing heat treatment temperature. It reduces from $10^{-5} \text{ g}\cdot\text{cm}^{-2}\cdot\text{min}^{-1}$ to $10^{-6} \text{ g}\cdot\text{cm}^{-2}\cdot\text{min}^{-1}$ for A1~A4 heat-treated glasses, while decreasing from $10^{-4} \text{ g}\cdot\text{cm}^{-2}\cdot\text{min}^{-1}$ to $10^{-5} \text{ g}\cdot\text{cm}^{-2}\cdot\text{min}^{-1}$ for A5 heat-treated glass. The great decrease in DR_{Acid} value indicates a significant improvement in acid resistance. It may be related to the apparent increase in the crystal volume fraction with increasing heat treatment temperature, as indicated by the XRD results. This phenomenon indicates that acid resistance can be greatly improved by controllable crystallization heat treatment on $\text{R}_2\text{O}-\text{Bi}_2\text{O}_3-\text{B}_2\text{O}_3-\text{SiO}_2$ base glass. Therefore, $\text{R}_2\text{O}-\text{Bi}_2\text{O}_3-\text{B}_2\text{O}_3-\text{SiO}_2$ glass-ceramic powder was used to prepare automotive glass enamel in order to significantly improve the acid resistance of the enamel.

SEM results of heated A4 samples and their SEM after corrosion (see Figure 9) have been taken as an example in order to further study the microstructure of the samples obtained by heating the same base glass at different heat treatment temperatures and to study the effect of acid corrosion on the surface microstructure of these samples. Micrographs of heated A4 samples before and after acid corrosion are shown in the a and b series of Figure 9, respectively. No crystals are observed in Figure 9a₁, indicating that the A4-1 sample is vitreous, which is consistent with its XRD identification result. A small number of star-shaped crystals are precipitated in the A4-2 sample (see Figure 9a₂), and these star-shaped crystals grow and increase in number and size in the A4-3 sample, as shown in Figure 9a₃. It can be presumed that the star-shaped crystals are $\text{Bi}_2\text{O}_2\text{SiO}_3$ crystals since this phase is the major crystalline phase in A4-2 and A4-3 samples, as indicated by the XRD result. As shown in Figure 9a₄, instead of star-shaped crystals, a large number of

intermeshing crystals are observed in A4-4 samples. They are $\text{Bi}_4\text{Si}_3\text{O}_{12}$ crystals since only the $\text{Bi}_4\text{Si}_3\text{O}_{12}$ phase is identified in this sample.

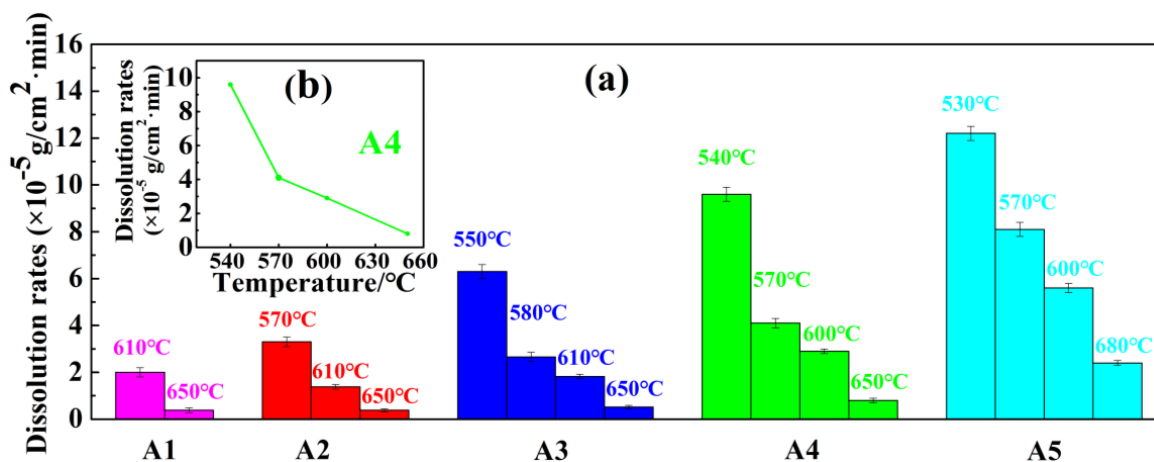


Figure 8. (a) Dissolution rates of all heat-treated glasses in acid solutions; (b) Dissolution rates of A4 heat-treated glasses in acid solutions.

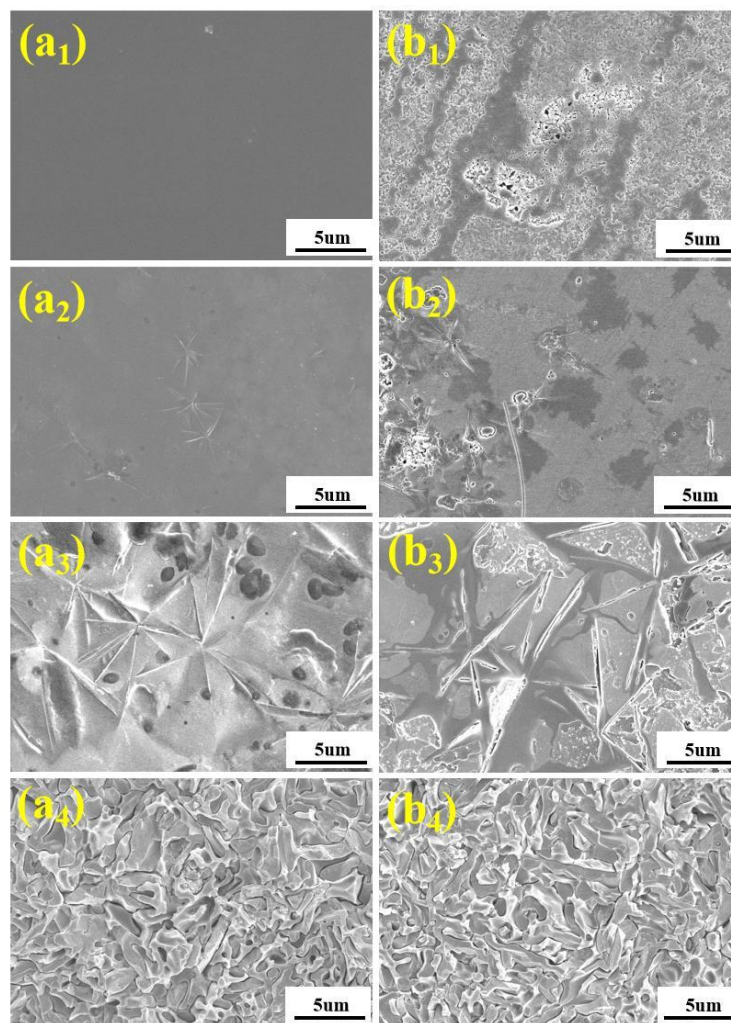


Figure 9. SEM of A4-1~A4-4 samples before (serial a) and after (serial b) corrosion in nitric acid solution. Among them, (a₁,b₁) correspond to sample A4-1, (a₂,b₂) correspond to sample A4-2, (a₃,b₃) correspond to sample A4-3, and (a₄,b₄) correspond to sample A4-4.

In comparison with micrographs of the a and b series in Figure 9, when the heat treatment temperature is below 600 °C, there is a great difference between the surface morphology of heated A4 base glass before and after corrosion, such as in the A4-1 and A4-2 samples. It may result from the high content of glassy phases in them. After the corrosion of the glassy phase, a large number of fine pits were formed (see Figure 9(b₁,b₂)), which led to a significant increase in the surface roughness. The actual surface area of the sample increased with increasing surface roughness, and the corrosion of A4-1 and A4-2 samples was ultimately accelerated. When the heat treatment temperature increased to 600 °C, corrosion was greatly slowed by the precipitation of a large number of crystals in the A4-3 sample. Corrosion also occurred on the glassy part of the A4-3 sample. As the heat treatment temperature increases to 650 °C, the volume fraction of crystals is quite high in the A4-4 sample. At the grain boundaries, there is a small amount of residual glassy phase. After corroding the surface of the A4-4 sample, it is difficult for a nitric acid solution to enter its interior and cause further corrosion. Thus, A4-4 has the highest acid resistance among these heated A4 base glasses.

In order to study the effect of crystallization of base glass on CTE, the CTE of A4-4 glass-ceramic was measured, and its CTE curve is shown in Figure 10. According to Figure 10, the $\alpha_{30-300\text{ °C}}$ value of A4-4 glass-ceramic is $8.19 \times 10^{-6}/\text{°C}$, which is lower than that of A4 base glass ($9.05 \times 10^{-6}/\text{°C}$). The CTE of A4-4 glass-ceramic matches the CTE of automotive glass. Therefore, A4-4 glass-ceramic powder was adopted to prepare automotive enamel in the present paper.

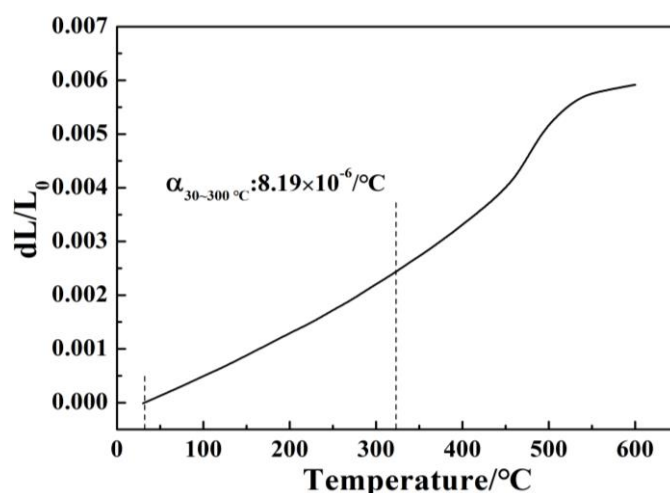


Figure 10. CTE curve of A4-4 glass-ceramics.

3.4. Preparation and Properties of Glass-Ceramic Enamel

A4-4 glass-ceramic powder was mixed with black pigment and varnish to prepare automobile glass enamel paste (see Figure 11). Photos of automobile glass printed with glass enamel and sintered are shown in Figure 12. Table 6 shows the performance parameters, such as acid resistance, adhesion, color, optical density, gloss, roughness, and surface tension, of our product and similar products on the market. The acid resistance of our automobile glass enamel is much higher than that of the similar product in the market because its DR_{Acid} value ($2.9 \times 10^{-6} \text{ g}\cdot\text{cm}^{-2}\cdot\text{min}^{-1}$) is an order of magnitude lower than that ($6.4 \times 10^{-5} \text{ g}\cdot\text{cm}^{-2}\cdot\text{min}^{-1}$) of the product in the market. The sintered enamel was cross-sectioned with a Cross-Cut Tester, and there was no peeling phenomenon, illustrating that its adhesion ISO grade was 0, which indicated that the enamel layer was fully sintered and firmly bonded to the automotive glass. The L value of our enamel is 6.39, which indicates good color, and its optical density (OD) value is 3.71, indicating low transmittance and strong shading ability. The G value of glossiness of our product is 6.5 Gs, which demonstrates that it is matte. Since the printing enamel area is the part where the automobile glass is installed and fixed, the roughness and surface tension will affect the

firmness of the automotive glass installation. The roughnesses Ra and Rz of our product are $0.624 \mu\text{m}$ and $4.393 \mu\text{m}$, respectively, and the surface tension σ is 44 mN/m . In sum, the indicators of our product meet the requirements of the current mainstream automobile manufacturers, and it has much higher acid resistance than commercial products.



Figure 11. Photo of glass enamel paste to be printed on automobile glass.

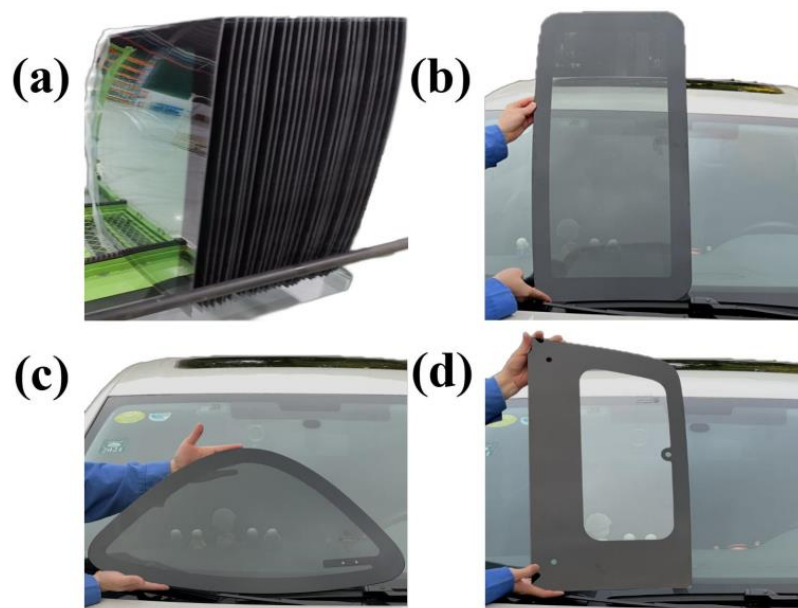


Figure 12. Photos of automobile glass printed with glass enamel and sintered: (a) front windshield; (b) sunroof windshield; and (c,d) side windshield.

Table 6. Properties of sintered enamel.

Properties	Our Products	Similar Product in Market
$DR_{Acid} (\text{g} \cdot \text{cm}^{-2} \cdot \text{min}^{-1})$	2.9×10^{-6}	6.4×10^{-5}
Adhesive force, (ISO grade)	0	0
Chroma (L , a , and b)	$L: 6.39, a: -0.08, b: -0.08$	$L: 6.17, a: -0.10, b: -0.09$
Optical density, (OD)	3.71	3.55
Glossiness, G (Gs)	6.5	7.8
Roughness, Ra, Rz (μm)	$Ra: 0.624$ $Rz: 4.393$	$Ra: 0.611$ $Rz: 4.256$
Surface tension, σ (mN/m)	44	44

4. Conclusions

- (1) For glasses in the $15R_2O-xBi_2O_3-10B_2O_3-(75-x)SiO_2$ system, their T_g , T_f , and S values decrease regularly, their crystallization ability is improved, their crystallization temperature range is widened, and the number of crystallization exothermic peaks varies from one to two or even three with increasing Bi_2O_3/SiO_2 ratio.
- (2) The three crystallization exothermic peaks (T_{p1} , T_{p2} , and T_{p3}) in the DTA curve of A4 base glass correspond to the crystallization of Bi_2SiO_5 , $Bi_2O_2SiO_3$, and $Bi_4Si_3O_{12}$ crystals, respectively. The crystallization activation energies of the three types of crystalline phases are 208.4 kJ/mol (E_{c1}), 169.4 kJ/mol (E_{c2}), and 263.6 kJ/mol (E_{c3}), respectively. The crystallization of A4 base glass is bulk crystallization.
- (3) When the crystallization temperature is in the range of 530–650 °C, the metastable Bi_2SiO_5 and $Bi_2O_2SiO_3$ crystalline phases are mainly precipitated. Above 650 °C, only $Bi_4Si_3O_{12}$ crystalline phases are precipitated, and $Bi_4Si_3O_{12}$ crystals are intermingled with each other. The crystallinity of the base glass increases significantly with the increase in heat treatment temperature. The CTE of the glass-ceramic is significantly lower than that of the corresponding base glass. DR_{Acid} values of the heat-treated base glasses are in the range of $10^{-5}\sim 10^{-6}$ g·cm⁻²·min⁻¹. In comparison with base glass, the DR_{Acid} values of base glass heated at temperatures higher than 650 °C decrease by an order of magnitude. It proves that increasing the heat treatment temperature is beneficial for improving the acid resistance of base glass. Enamel was prepared by mixing A4-4 glass-ceramic powder with copper-chromium black and varnish, then printed on automotive glass substrates, and then sintered. The indicators of our product meet the requirements of the current mainstream automobile manufacturers, and it has much higher acid resistance than commercial products.

Author Contributions: Conceptualization, T.Z.; Methodology, T.Z., W.W. and J.Z.; Validation, K.L. and W.D.; Investigation, W.W.; Resources, L.L.; Data curation, T.Z.; Writing—original draft, T.Z.; Writing—review & editing, T.Z.; Visualization, Q.B.; Supervision, H.X.; Project administration, K.L., Q.B. and J.Z.; Funding acquisition, W.D. All authors have read and agreed to the published version of the manuscript.

Funding: We would like to express our gratitude for the financial support from the Educational Major Project of Jiangxi Province in China (No. GJJ201301), the Major Project of Jingdezhen Ceramic Industry (No. 2021ZDGG004), the Jingdezhen Technology Bureau Grant (No. 2021GYZD009-18), the Jiangxi Province Key R&D Program in China (No. 20202BBE53012), the 2021 Open Project “State Key Laboratory of Silicon Materials” (No. SKL2021-04), and Jingdezhen Technology Bureau (No. 20224GY008-16).

Data Availability Statement: The raw data required to reproduce these findings cannot be shared at this time as the data also forms part of an ongoing study.

Conflicts of Interest: The authors declare no conflict of interest.

References

1. Wang, N.; Pan, H.Z.; Zheng, W.H. Assessment of the incentives on electric vehicle promotion in China. *Transport. Res. A Pol.* **2017**, *101*, 177–189. [[CrossRef](#)]
2. Gong, H.M.; Wang, M.; Wang, H.W. New energy vehicles in China: Policies, demonstration, and progress. *Mitig. Adapt. Strateg. Glob. Chang.* **2013**, *18*, 207–228. [[CrossRef](#)]
3. Li, Y.S.; Kong, X.X.; Zhang, M. Industrial upgrading in global production networks: The case of the Chinese automotive industry. *Asia Pac. Bus. Rev.* **2016**, *22*, 21–37. [[CrossRef](#)]
4. Liu, B.C.; Song, C.Y.; Wang, Q.S.; Zhang, X.M.; Chen, J.L.; Lund, H.; Kaiser, M.J. Research on regional differences of China’s new energy vehicles promotion policies: A perspective of sales volume forecasting. *Energy* **2022**, *248*, 123541. [[CrossRef](#)]
5. Rossi, S.; Russo, F.; Calovi, M. Durability of vitreous enamel coatings and their resistance to abrasion, chemicals, and corrosion: A review. *J. Coat. Technol. Res.* **2021**, *18*, 39–52. [[CrossRef](#)]
6. Malnieks, K.; Mezinskis, G.; Pavlovska, I.; Bidermanis, L.; Pludons, A. Black enamel for concentrated solar-power receivers. *Ceram. Int.* **2014**, *40*, 13321–13327. [[CrossRef](#)]

7. Ren, B.Y.; Luo, D.S.; Dai, Y.X.; Tong, Z. Preparation and properties of anti-adhering and acid-resistant tempered glass ink applied to automotive. *J. South China Univ. Technol.* **2013**, *41*, 112–116+132.
8. Mahdi, S. Organic/inorganic coatings cured by ultraviolet light and moisture for automotive glass. *SAE Int. J. Mater. Manuf.* **2012**, *5*, 499–502. [[CrossRef](#)]
9. Peng, Y.; Zhang, Y. Preparation of highly dispersible glass frit powders and its application in ink-jet printing ink. *J. Eur. Ceram. Soc.* **2020**, *40*, 3489–3493. [[CrossRef](#)]
10. Jiao, J.X.; Yang, M.; Li, J.W.; Xiong, D.H.; Li, H. A novel high reflective glass-ceramic ink with Bi₂Ti₂O₇ nanocrystals used for the photovoltaic glass backplane. *J. Eur. Ceram. Soc.* **2023**, *43*, 3630–3636. [[CrossRef](#)]
11. Kulikova, O.V.; Shchegoleva, N.E.; Lebedeva, Y.E.; Vaganova, M.L.; Chainikova, A.S. Insulating Enamel Based on Lead-Borate Glass. *Glass Ceram.* **2022**, *78*, 436–441. [[CrossRef](#)]
12. Schalm, O.; Van der Linden, V.; Frederickx, P.; Luyten, S.; Van der Snickt, G.; Caen, J.; Schryvers, D.; Janssens, K.; Cornelis, E.; Van Dyck, D.; et al. Enamels in stained glass windows: Preparation, chemical composition, microstructure and causes of deterioration. *Spectrochim. Acta B* **2009**, *64*, 812–820. [[CrossRef](#)]
13. Yin, S.H.; Wang, H.; Wang, S.F.; Zhang, J.; Zhu, Y.Z. Effect of B₂O₃ on the radiation shielding performance of telluride lead glass system. *Crystals* **2022**, *12*, 178. [[CrossRef](#)]
14. Butenkov, D.A.; Runina, K.I.; Petrova, O.B. Synthesis and properties of Nd-doped chlorofluorosilicate lead glasses. *Glass Ceram.* **2021**, *78*, 135–139. [[CrossRef](#)]
15. Al-Hadeethi, Y.; Tijani, S.A. The use of lead-free transparent 50BaO-(50-x) borosilicate-xBi₂O₃ glass system as radiation shields in nuclear medicine. *J. Alloys Compd.* **2019**, *803*, 625–630. [[CrossRef](#)]
16. Tijani, S.A.; Al-Hadeethi, Y. The influence of TeO₂ and Bi₂O₃ on the shielding ability of lead-free transparent bismuth tellurite glass at low gamma energy range. *Ceram. Int.* **2019**, *45*, 23572–23577. [[CrossRef](#)]
17. Halimah, M.K.; Azuraida, A.; Ishak, M.; Hasnimulyati, L. Influence of bismuth oxide on gamma radiation shielding properties of boro-tellurite glass. *J. Non-Cryst. Solids* **2019**, *512*, 140–147. [[CrossRef](#)]
18. Al-Hadeethi, Y.; Sayyed, M.I. BaO-Li₂O-B₂O₃ glass systems: Potential utilization in gamma radiation protection. *Prog. Nucl. Energy* **2020**, *129*, 103511. [[CrossRef](#)]
19. Luhar, S.; Cheng, T.; Nicolaidis, D.; Luhar, I.; Panias, D.; Sakkas, K. Valorisation of glass wastes for the development of geopolymer composites—Durability, thermal and microstructural properties: A review. *Constr. Build. Mater.* **2019**, *222*, 673–687. [[CrossRef](#)]
20. Stalin, S.; Gaikwad, D.K.; Al-Buriah, M.S.; Srinivasu, C.; Ahmed, S.A.; Tekin, H.O.; Rahman, S. Influence of Bi₂O₃/WO₃ substitution on the optical, mechanical, chemical durability and gamma ray shielding properties of lithium-borate glasses. *Ceram. Int.* **2021**, *47*, 5286–5299. [[CrossRef](#)]
21. Kalio, A.; Leibinger, M.; Filipovic, A.; Krüger, K.; Glatthaar, M.; Wilde, J. Development of lead-free silver ink for front contact metallization. *Sol. Energy Mater. Sol. Cells* **2012**, *106*, 51–54. [[CrossRef](#)]
22. Adeyemi, J.; Onwudiwe, D. Chemistry and some biological potential of bismuth and antimony dithiocarbamate complexes. *Molecules* **2020**, *25*, 305. [[CrossRef](#)] [[PubMed](#)]
23. Maeder, T. Review of Bi₂O₃ based glasses for electronics and related applications. *Int. Mater. Rev.* **2013**, *58*, 3–40. [[CrossRef](#)]
24. Hussein, E.M.A.; Madbouly, A.M.; El Alaily, N.A. Gamma ray interaction of optical, chemical, physical behavior of bismuth silicate glasses and their radiation shielding proficiency using Phy-X/PSD program. *J. Non-Cryst. Solids* **2021**, *570*, 121021. [[CrossRef](#)]
25. Laourayed, M.; El Moudane, M.; Khachani, M.; Boudalia, M.; Guenbour, A.; Bellaouchou, A.; Tabyaoui, M. Effect of the Bi₂O₃ on the thermal, structural and chemical durability of some bismuth niobium phosphate glasses. *Mater. Today* **2019**, *13*, 974–981. [[CrossRef](#)]
26. Emlemdi, H. Durable Functional Glass Enamel Coating for Automotive Applications. U.S. Patent 7528084, 5 May 2009.
27. Singh, S.K.; Sakoske, G.E.; Klimas, D. Glass Enamel for Automotive Applications. U.S. Patent 20150013390, 15 January 2015.
28. Li, S.; Zhang, J.; Li, M.M.; Liu, J.; Wang, X.Y.; Mei, X.H.; Zhang, Y. Study on preparation and properties of boron bismuth/fluorooxy glass and glass-ceramics. *J. Non-Cryst. Solids* **2021**, *561*, 120749. [[CrossRef](#)]
29. El-Rehim, A.F.; Shaaban, K.S.; Zahran, H.Y.; Yahia, I.S.; Ali, A.M.; Halaka, M.M.A.; Makhlof, S.A.; Wahab, E.A.A.; Shaaban, E.R. Structural and mechanical properties of Lithium bismuth borate glasses containing molybdenum (LBBM) together with their glass-ceramics. *J. Inorg. Organomet. Polym. Mater.* **2021**, *31*, 1057–1065. [[CrossRef](#)]
30. Mahmoud, M.M.; Folz, D.C.; Suchicital, C.T.; Clark, D. Estimate of the crystallization volume fraction in lithium disilicate glass-ceramics using Fourier transform infrared reflectance spectroscopy. *J. Eur. Ceram. Soc.* **2015**, *35*, 597–604. [[CrossRef](#)]
31. Plekhovich, A.D.; Kut'in, A.M.; Rostokina, E.E.; Komshina, M.E.; Balueva, K.V.; Ignatova, K.F.; Shiryaev, V.S. Controlled crystallization of BaO-B₂O₃-Bi₂O₃ Glass in the temperature range of a supercooled melt in the presence of additional nucleation centers. *J. Non-Cryst. Solids* **2022**, *588*, 121629. [[CrossRef](#)]
32. Yang, Y.B.; Wu, L.; Teng, Y.C.; Jiang, F.; Lei, J.; Chen, H.; Cheng, J.H. Effect of ZnO content on microstructure, crystallization behavior, and thermal properties of xZnO-30B₂O₃-(65-x) Bi₂O₃-5BaO glass. *J. Non-Cryst. Solids* **2019**, *511*, 29–35. [[CrossRef](#)]
33. Wu, Z.L.; Zhang, M.; Zhang, C.Y.; Meng, F.C.; Lin, H.X. Effect of SrO Content on Structure, Thermal Properties and Chemical Stability of Bi₂O₃-B₂O₃-ZnO-SrO Low-melting Glass for Si-Al Alloy Package. *J. Wuhan Univ. Technol.* **2020**, *35*, 368–376. [[CrossRef](#)]
34. Yang, J.K.; Liang, B.; Zhao, M.J.; Gao, Y.; Zhang, F.C.; Zhao, H.L. Reference of Temperature and Time during tempering process for non-stoichiometric FTO films. *Sci. Rep.* **2015**, *5*, 15001. [[CrossRef](#)] [[PubMed](#)]

35. Hussein, E.M.A.; Madbouly, A.M.; Eldin, F.M.E.; ElAlaily, N.A. Evaluation of physical and radiation shielding properties of $\text{Bi}_2\text{O}_3\text{-B}_2\text{O}_3$ glass doped transition metals ions. *Mater. Chem. Phys.* **2021**, *261*, 124212. [[CrossRef](#)]
36. Kaur, K.; Singh, K.J.; Anand, V. Structural properties of $\text{Bi}_2\text{O}_3\text{-B}_2\text{O}_3\text{-SiO}_2\text{-Na}_2\text{O}$ glasses for gamma ray shielding applications. *Radiat. Phys. Chem.* **2016**, *120*, 63–72. [[CrossRef](#)]
37. Dararutana, P.; Duchaneephet, J.; Pongkrapan, S.; Sirikulrat, N.; Wathanakul, P. Effect of Bi_2O_3 content on optical and radiation shielding properties of $(\text{Na}_2\text{O}, \text{K}_2\text{O})\text{-SiO}_2\text{-CaO-Al}_2\text{O}_3\text{-B}_2\text{O}_3$ glass system. *Optoelectron. Adv. Mat.* **2009**, *3*, 525–527.
38. Xu, J.J.; Lin, P.P.; Chen, Q.Q.; Zhao, X.; He, P.; Lin, T.S.; Jiang, C.L.; Liu, Y.; Liu, H.Z.; Long, W.M. Evolutionary mechanism of YBO_3 whisker and its effect on the properties of YIG ferrite joint brazed by $\text{Bi}_2\text{O}_3\text{-B}_2\text{O}_3\text{-SiO}_2\text{-ZnO}$ glass. *Ceram. Int.* **2021**, *47*, 973–983. [[CrossRef](#)]
39. Popov, A.I.; Kotomin, E.A.; Maier, J. Basic properties of the F-type centers in halides, oxides and perovskites. *Nucl. Instrum. Methods Phys. Res. B* **2010**, *268*, 3084–3089. [[CrossRef](#)]
40. Luchechko, A.; Vasylytsiv, V.; Kostyk, L.; Tsvetkova, O.; Popov, A.I. Shallow and deep trap levels in X-ray irradiated $\beta\text{-Ga}_2\text{O}_3$: Mg. *Nucl. Instrum. Meth. B* **2019**, *441*, 12–17. [[CrossRef](#)]
41. Klym, H.; Ingram, A.; Shpotyuk, O.; Hotra, O.; Popov, A.I. Positron trapping defects in free-volume investigation of Ge–Ga–S–CsCl glasses. *Radiat. Meas.* **2016**, *90*, 117–121. [[CrossRef](#)]
42. Li, X.Y.; Xiao, Z.H.; He, Y.T.; Wang, Y.Q.; Luo, J.Z.; Shi, J.J.; Huang, Q.; Kong, L.B. Crystallization behavior, structure and properties of glasses in $\text{SrO-Fe}_2\text{O}_3\text{-P}_2\text{O}_5$ system. *J. Non-Cryst. Solids* **2019**, *523*, 119588. [[CrossRef](#)]
43. Qiang, L.Y.; Zhang, X.Z.; Ai, Y.Z.T.; Zhuan, Y.; Sheng, J.; Zhao, H.Y.; Ni, J.X.; Yang, K. Crystallization behavior and thermal stability mechanism of plasma sprayed $\text{Al}_2\text{O}_3\text{-GAP}$ amorphous ceramic coatings. *J. Eur. Ceram. Soc.* **2022**, *42*, 2018–2121. [[CrossRef](#)]
44. Jiang, H.R.; Hu, J.Y.; Neuber, N.; Bochtler, B.; Adam, B.; Riegler, S.S.; Frey, M.; Ruschel, L.; Lu, W.F.; Feng, A.H.; et al. Effect of sulfur on the glass-forming ability, phase transformation, and thermal stability of Cu–Zr–Al bulk metallic glass. *Acta Mater.* **2021**, *212*, 116923. [[CrossRef](#)]
45. Mohammed, A.; Lakshminarayana, G.; Baki, S.O.; Bashar, K.A.; Kityk, I.V.; Mahdi, M.A. Optical and dielectric studies for $\text{Tb}^{3+}/\text{Sm}^{3+}$ co-doped borate glasses for solid-state lighting applications. *Opt. Mater.* **2018**, *86*, 387–393. [[CrossRef](#)]
46. Çelikbilek Ersundu, M.; Ersundu, A.E. Structure and crystallization kinetics of lithium tellurite glasses. *J. Non-Cryst. Solids* **2016**, *453*, 150–157. [[CrossRef](#)]
47. Wang, S.H.; Li, X.N.; Wang, C.; Bai, M.M.; Zhou, X.J.; Zhang, X.Z.; Wang, Y.Q. Anorthite-based transparent glass-ceramic glaze for ceramic tiles: Preparation and crystallization mechanism. *J. Eur. Ceram. Soc.* **2022**, *42*, 1132–1140. [[CrossRef](#)]
48. Baranowska, A.; Leśniak, M.; Kochanowicz, M.; Żmojda, J.; Miluski, P.; Dorosz, D. Crystallization kinetics and structural properties of the 45S5 bioactive glass and glass-ceramic fiber doped with Eu^{3+} . *Materials* **2020**, *13*, 1281. [[CrossRef](#)]
49. Hivrekar, M.M.; Sable, D.B.; Solunke, M.B.; Jadhav, K.M. Network structure analysis of modifier CdO doped sodium borate glass using FTIR and Raman spectroscopy. *J. Non-Cryst. Solids* **2017**, *474*, 58–65. [[CrossRef](#)]
50. Shi, X.Z.; Gu, Y.; Liu, T.Y.; Jiang, Z.H.; Li, R.; Zeng, F.H. Effect of different $\text{P}_2\text{O}_5/\text{SnF}_2$ ratios on the structure and properties of phosphate glass. *J. Non-Cryst. Solids* **2022**, *578*, 121350. [[CrossRef](#)]
51. Saritha, D.; Markandeya, Y.; Salagram, M.; Vithal, M.; Singh, A.K.; Bhikshamaiah, G. Effect of Bi_2O_3 on physical, optical and structural studies of $\text{ZnO-Bi}_2\text{O}_3\text{-B}_2\text{O}_3$ glasses. *J. Non-Cryst. Solids* **2008**, *354*, 5573–5579. [[CrossRef](#)]
52. Rada, S.; Pascuta, P.; Bosca, M.; Pop, L.; Culea, E. Structural properties of the boro-bismuthate glasses containing gadolinium ions. *Vib. Spectrosc.* **2008**, *48*, 255–258. [[CrossRef](#)]
53. Emami, S.; Martins, J.; Andrade, L.; Mendes, J.; Mendes, A. Low temperature hermetic laser-assisted glass frit encapsulation of soda-lime glass substrates. *Opt. Lasers Eng.* **2017**, *96*, 107–116. [[CrossRef](#)]
54. Lei, W.C.; Luo, Z.W.; He, Y.; Zhang, P.; Liu, S.X.; Lu, A.X. ZrO_2 -doped transparent glass-ceramics embedding ZnO nano-crystalline with enhanced defect emission for potential yellow-light emitter applications. *Ceram. Int.* **2021**, *47*, 35073–35080. [[CrossRef](#)]
55. Ray, C.S.; Yang, Q.Z.; Huang, W.H.; Day, D.E. Surface and internal crystallization in glasses as determined by differential thermal analysis. *J. Am. Ceram. Soc.* **1996**, *79*, 3155–3160. [[CrossRef](#)]
56. Todea, M.; Turcu, R.V.F.; Vasilescu, M.; Trandafir, D.L.; Simon, S. Structural characterization of heavy metal $\text{SiO}_2\text{-Bi}_2\text{O}_3$ glasses and glass-ceramics. *J. Non-Cryst. Solids* **2016**, *432*, 271–276. [[CrossRef](#)]
57. Guo, H.W.; Wang, X.F.; Gao, D.N. Non-isothermal crystallization kinetics and phase transformation of $\text{Bi}_2\text{O}_3\text{-SiO}_2$ glass-ceramics. *Sci. Sinter.* **2011**, *43*, 353–362. [[CrossRef](#)]

Disclaimer/Publisher’s Note: The statements, opinions and data contained in all publications are solely those of the individual author(s) and contributor(s) and not of MDPI and/or the editor(s). MDPI and/or the editor(s) disclaim responsibility for any injury to people or property resulting from any ideas, methods, instructions or products referred to in the content.